NIH-PA Author Manuscript

Synthesis, Characterization and Study of Octanuclear Iron-Oxo Clusters Containing a Redox-Active Fe$_4$O$_4$-Cubane Core

Peter Baran[a,b], Roman Boča[c], Indranil Chakraborty[a], John Giapintzakis[d], Radovan Herchel[e,f], Qing Huang[a], John E. McGrady[g], Raphael G. Raptis[a], Yiannis Sanakis[h], and Athanasios Simopoulos[h]

a *Department of Chemistry and the Institute of Functional Nanomaterials, University of Puerto Rico, San Juan, PR 00931-3346*

c *Department of Inorganic Chemistry, Slovak University of Technology, SK-812 37 Bratislava, Slovakia*

d *Department of Mechanical & Manufacturing Eng., University of Cyprus, 75 Kallipoleos Ave., PO Box 20537, 1678 Nicosia, Cyprus*

e *Department of Chemistry, University of SS. Cyril and Methodius, Trnava, SK-91701, Slovakia*

f *Department of Inorganic Chemistry, Palacký University, K ížkovského 10, CZ-77147 Olomouc, Czech Republic*

g *WestCHEM, Department of Chemistry, University of Glasgow, Glasgow G12 8QQ, U.K.*

h *Institute of Materials Science, NCSR "Demokritos", 15310 Aghia Paraskevi, Athens, Greece*

Abstract

A one pot synthetic procedure yields the octanuclear Fe^{III}-complexes Fe$_8$(μ_4-O)$_4$(μ-pz*)$_{12}$X$_4$, where X = Cl and pz* = pyrazolate anion (pz = C$_3$H$_3$N$_2^-$) (**1**), 4-Cl-pz (**2**) and 4-Me-pz (**3**), or X = Br and pz* = pz (**4**). The crystal structures of complexes **1** – **4**, determined by X-ray diffraction, show an Fe$_4$O$_4$-cubane core encapsulated in a shell composed of four interwoven Fe(μ-pz*)$_3$X-units. Complexes **1** – **4** have been characterized by ^{1}H-nmr, infrared and Raman spectroscopy. Mössbauer spectroscopic analysis distinguishes the cubane and outer Fe^{III}-centers by their different isomer shift and quadrupole splitting values. Electrochemical analyses by cyclic voltammetry show four consecutive, closely spaced, reversible reduction processes for each one of the four complexes. Magnetic susceptibility studies, corroborated by Density Functional Theory calculations, reveal weak antiferromagnetic coupling among the four cubane Fe-centers and strong antiferromagnetic coupling between cubane and outer Fe-atoms of **1**. The structural similarity between the antiferromagnetic Fe$_8$(μ_4-O)$_4$-core of **1** – **4** and the also antiferromagnetic units contained in the minerals ferrihydrite and maghemite is demonstrated by X-ray and Mössbauer data.

Introduction

We describe here the syntheses, structural characterization and physical properties of four octanuclear Fe^{III}-complexes containing a common redox-active Fe$_4$O$_4$-cubane core, along with arguments supporting the suggestion that a future discovery of an electron-transfer protein with a Fe$_4$O$_4$ active-center is not an unreasonable expectation. Iron-sulfur cubanes able to cycle between two (or more) oxidation states constitute the electron-transfer components of several

Correspondence to: Raphael G. Raptis.

[b]Present address: Department of Chemistry, Juniata College, Huntingdon, PA 16652.

ferredoxins involved in biological redox processes.[1] Consequently, the study of model complexes containing Fe_4S_4-cubane cores has been a central theme of bioinorganic Chemistry over the last thirty years.[2] While no redox-active Fe_4O_4-cubane core has been unequivocally characterized in a metalloprotein, examples of protein active-centers consisting of Fe/O-containing cubanes are known: A unique redox-active $Fe_4O_2S_2$-cluster has been recognized in the active core of hybrid cluster protein (HCP, formerly termed prismane protein).[3] The HCP of *E. coli* catalyses the 2-electron reduction of hydroxylamine to ammonia.[4] Similar hydroxylamine reductase activity results from the insertion of Fe into the vacant site of Ni-deficient carbon monoxide dehydrogenase (Ni-CODH, with an Fe_3NiO_4-cubane core[5]), creating in a sense Fe-CODH.[4] In a recent Fe K-edge X-ray absorption spectroscopic study, Hogdson *et al.* have shown that a protein isolated from the blood of *Perophora annectens* contains a Fe_4O_4-core in either a cubane or a ladder arrangement, with the authors leaning towards the cubane assignment.[6] The absence of a well characterized Fe_4O_4 electron-transfer protein cannot simply be due to a scarcity of components - oxo and hydroxo ligands are readily available in Nature and metal-oxo active cores are present in numerous metalloproteins, including the Fe_2O_2-cores of ribonucleotide reductase, purple acid phosphatase and soluble methane monooxygenase.[7] A structure containing fused cubanes with 6-coordinate Fe-centers is also one of the possible models consistent with the EXAFS studies of ferritin, the mammalian iron-storage protein, containing a few thousand Fe^{III}-centers.[8]

Several synthetic iron complexes containing the Fe_4O_4-motif with Fe^{II} or mixed-valent $Fe^{II/III}$ centers have been reported to date.[9-19] These are either Fe_4O_4-carboxylate complexes, or larger polynuclear carboxylates containing Fe_4O_4-units. Our contribution to this field consists of a preliminary account of the simple, one-pot synthesis and structural characterization of an octanuclear Fe^{III}-cluster, $Fe_8(\mu_4\text{-O})_4(\mu\text{-pz})_{12}Cl_4$ (pz = pyrazolato anion, $C_3H_3N_2^-$), **1**, containing an $Fe^{III}_4O_4$-cubane core.[20] The latter, along with the recently characterized $[Fe_8^{III}O_4(sao)_8(py)_4]\cdot4py$,[19] (sao = salicylaldoximato; py = pyridine) constitute the only examples of all-ferric oxo cubanes. Furthermore, we have shown that **1** can reversibly accept up to four electrons in four consecutive electrochemical steps, spaced approximately 0.35 V from each other.[20] The first reduction occurs at the modest potential of −0.43 V, while the fourth one lies at −1.38 V (versus Fc^+/Fc); compound **1** can shuttle four electrons across a redox potential window of ~1.1 V. Consequently, the redox properties of **1** show it to be a more efficient electron-transfer agent than any of the naturally occurring, or synthetic, Fe_4S_4 clusters.[21] The question that arises, then, is the following: why has Nature apparently ignored such a simple and efficient redox catalyst in favor of its sulfur analogues? It can be argued that Nature's preference for sulfur-based cubanes arises simply because ferredoxins are believed to have evolved during a pre-photosynthetic geological period in an anoxic, sulfur-rich environment.[22] However, proteins are able to mutate to adapt to their changing environment by switching from depleted to readily available elements. For example, oxygen-for-sulfur substitution is known in the cases of rubredoxin from *c. pasteurianum*, which switches from an $Fe(S\text{-cyst})_4$-core to a $Fe(S\text{-cyst})_3(OH)$ one, while the $Fe_4(S\text{-cys})_4$ active center of *c. vinosum* switches to $Fe_4(S\text{-cys})_3(O\text{-ser})$.[23] Consequently, it is quite possible that an initially sulfur-based multi-iron protein may later have evolved into an oxygen-based one. Noting also that many metalloproteins remain to be discovered, Lippard *et al.* and we have suggested that an electron-transfer protein with a Fe_4O_4 active center may be recognized in the future.[15,20]

Continuing our studies of the octanuclear cluster **1**, we report here the magnetic susceptibility, Density Functional Theory (DFT) study, infrared, Raman, ^{1}H-NMR and Mössbauer spectroscopic characterization of **1**, along with the syntheses, structural characterization and electrochemical studies of its substituted-pyrazole derivatives, $Fe_8(\mu_4\text{-O})_4(\mu\text{-pz*})_{12}Cl_4$, where pz* = 4-Cl-pz (**2**) and 4-Me-pz (**3**), along with the bromo-analogue, $Fe_8(\mu_4\text{-O})_4(\mu\text{-pz})_{12}Br_4$, **4**. These studies probe the electronic structure of the Fe_4O_4 motif and define its spectroscopic and magnetic "fingerprint", facilitating its possible future recognition in Nature.

Experimental Section

FeCl$_3$, FeBr$_3$, pyrazole (pzH), 4-Me-pyrazole (4-Me-pzH), NaH and Et$_3$N were obtained from commercial sources and used as received. Napz was prepared from pzH and NaH. 4-Cl-pyrazole (4-Cl-pzH) was prepared by a literature method.[24] Solvents (CH$_2$Cl$_2$, methanol, acetone, diethyl ether, tetrahydrofuran, hexane) were purified by standard methods.[25]

[Fe$_8$(μ$_4$-O)$_4$(μ-pz)$_{12}$Cl$_4$] (1)

To a suspension of FeCl$_3$ (3.120g, 19.23 mmol) in CH$_2$Cl$_2$ (200 ml) was added Napz (2.598g, 28.85 mmol) under an Ar atmosphere with stirring. The reaction mixture was exposed to air, sealed and kept under stirring at ambient temperature for 20 h. The resulting dark brown solution was then filtered, the filtrate was collected in a round-bottomed flask and the solvent was evaporated under reduced pressure. The resulting solid was dissolved in the minimum amount of CH$_2$Cl$_2$ with which was charged a silica gel chromatographic column (60-120 mesh, Aldrich) prepared with toluene. The dark orange portion eluted with CH$_2$Cl$_2$ was collected in a round-bottomed flask, the solvent was removed in a rotary evaporator, the product was air dried, then washed with dry MeOH and then dried in a vacuum desicator over CaCl$_2$. X-ray quality dark red crystals were obtained upon recrystallization by slow Et$_2$O-vapor diffusion into a CH$_2$Cl$_2$ solution of **1**. Yield 1.07 g (30%). UV/VIS/NIR (CH$_2$Cl$_2$): λ_{max} = 360 nm (27788 cm^{-1}), ε = 37000 cm^{-1} mol^{-1} dm^3. IR (KBr disk): 1490(m), 1417(m), 1362(vs), 1268(vs), 1170 (m), 1145(w), 1045(vs), 963(w), 915(w), 895(w), 871(w), 764(s), 615(m), 556(w), 478 (vs, br Fe-O). ^{1}H NMR (δ, ppm, CDCl$_3$): 42.2 (s, 1 H, ^{4}H), 10.5 (s, 1 H, ^{3}H), 3.5 (s, 1 H, ^{5}H).

[Fe$_8$(μ$_4$-O)$_4$(μ-4-Cl-pz)$_{12}$Cl$_4$] (2)

To a suspension of FeCl$_3$ (0.586 g, 3.61 mmol) in CH$_2$Cl$_2$ (200mL) was added 4-Cl-pyrazole (0.556g, 5.42 mmol) under an Ar atmosphere with stirring. To the resulting solution, Et$_3$N (0.629 ml, 4.52 mmol) was added dropwise with stirring under Ar. Then the reaction mixture was exposed to air, sealed and kept under stirring at room temperature for 20 h. Then the resulting dark brown solution was filtered and worked-up in similar way as described for **1**. X-ray quality single crystals were grown by slow evaporation of a CH$_2$Cl$_2$ solution of **2**. Yield: 2.70 g (40%). Anal. Calcd for C$_{40}$H$_{40}$Cl$_{18}$Fe$_8$N$_{24}$O$_4$: C, 22.36; H, 1.88; N, 15.64. Found: C, 22.61; H, 1.93; N, 15.36. UV/VIS/NIR (CH$_2$Cl$_2$): λ_{max} = 363 nm (27639 cm^{-1}). The ^{18}O-isotopically labeled complex **2** was prepared as above, except that 0.05 mL H$_2$^{18}O was added to the reaction mixture under an Ar atmosphere, instead of exposing it to the air. IR (KBr disk): 1384(m), 1354(m), 1315(w), 1297(vs), 1217(w), 1189(s), 1151(w), 1041(vs), 993(w), 967(m), 855(w), 608(s), 528(w), 475(vs, br Fe-O). ^{1}H NMR (δ, ppm, CDCl$_3$): 13.7 (s, 1 H, ^{3}H), 8.6 (s, 1 H, ^{5}H).

[Fe$_8$(μ$_4$-O)$_4$(μ-4-Me-pz)$_{12}$Cl$_4$] (3)

To a suspension of FeCl$_3$ (0. 967 g, 5.96 mmol) in CH$_2$Cl$_2$ (200 ml) was added 4-Me-pyrazole (1.48ml, 17.9 mmol) under an Ar atmosphere with stirring. To the resulting solution, Et$_3$N (2.08 ml, 14.9 mmol) was added dropwise with stirring under Ar. Then the reaction mixture was exposed to air, sealed and kept under stirring at room temperature for 20 h. Then the resulting dark brown solution was filtered and worked-up in similar way as described for **1** and **2**. Yield: 5.59 g (57%). Anal. Calcd for C$_{48}$H$_{60}$Cl$_4$Fe$_8$N$_{24}$O$_4$: C, 35.46; H, 3.72; N, 20.68. Found: C, 36.14; H, 4.04; N, 20.53. UV/VIS/NIR (CH$_2$Cl$_2$): λ_{max} = 376 nm (26848 cm^{-1}). IR (KBr disk):1389(w), 1355(s), 1311(s), 1216(w), 1165(m), 1054(vs), 1012(m), 846(m), 674 (m), 617(s), 555(w), 478(vs, br Fe-O). ^{1}H NMR (δ, ppm, CDCl$_3$): 27.7 (s, 3 H, Me), 8.6 (s, 1 H, ^{3}H), 3.8 (s, 1 H, ^{5}H).

$[Fe_8(\mu_4\text{-}O)_4(\mu\text{-}pz)_{12}Br_4]$ (4)

To a suspension of $FeBr_3$ (0.371 g, 1.26 mmol) in CH_2Cl_2 (15 ml) prepared under argon atmosphere was added solid pyrazole (0.256 g, 3.77 mmol) under air with stirring. To the red solution was added drop wise with stirring triethylamine (0.437 ml, 3.14 mmol). After stirring for 10 min, the mixture was filtered and filtrate was placed into a Schlenk tube and stirred under nitrogen for 6 days. The volume of the reaction mixture was reduced to 5 mL under vacuum, stirred overnight and filtered under nitrogen. The filtrate was evaporated to dryness, washed with methanol (22 ml) and recrystallized from diethyl ether (40 ml) and subsequently from CH_2Cl_2 (6 ml). Product was collected by filtration, washed with methanol, and dried. Yield: 0.821 g (40%). Anal. Calcd for $C_{36}H_{36}Br_4Fe_8N_{24}O_4$: C, 26.44; H, 2.22; N, 20.56. Found: C, 26.24; H, 2.37; N, 20.38. UV/VIS/NIR (CH_2Cl_2): λ_{max} = 399 nm (25728 cm^{-1}). IR (KBr disk): 1491(m), 1417(m), 1362(s), 1266(s), 1230(w), 1168(s), 1076(w), 1044(vs), 764 (s), 614(m), 552(w), 477(vs, br Fe-O). ^{1}H NMR (δ, ppm, $CDCl_3$): 42.9 (s, 1 H, [4]H), 10.7 (s, 1 H, ^{3}H), 1.0 (s, 1 H, [5]H).

Physical Measurements

Electronic spectra of the complexes in solution were recorded on Varian CARY 500 Scan in the 200-2000 nm range. Infrared spectra (KBR and/or polyethylene pellets) were recorded on Nicolet 750 FTIR spectrophotometers. The Raman spectra of the solid samples in the form of powders were recorded at room temperature in backscattering geometry. Excitation at 488 nm was provided by a Lexel 95 Argon ion laser system, with applied laser power of 5–10 mW. The scattered light was dispersed by a triple-grating spectrometer (Jobin-Yvon, Edison, NJ) and the spectra were recorded by a liquid nitrogen cooled CCD camera (CCD3000 from Jobin-Yvon). ^{1}H NMR were recorded on Bruker ADVANCE DRX-500 spectrometer. Mössbauer spectra were recorded with powdered samples of **1** with a constant-acceleration conventional spectrometer with a source of [57]Co (Rh matrix). Spectra in the 4.2-300 K range were obtained using Oxford cryostats. One cryostat was equipped with a superconducting magnet with the magnetic field perpendicular to the γ-rays. The spectra were analyzed by using the program WMOSS (Web Research, Edina, MN). Isomer shift values (δ) are reported relative to iron foil at 293 K. Temperature dependent (2-298 K) magnetic susceptibility data were recorded on SQUID magnetometer in an external magnetic field of 1 T. A correction to the underlying diamagnetism was estimated on the basis of Pascal constants as $\chi_{dia} = -7.45 \times 10^{-9}$ m^{3}mol^{-1}.[26] The effective magnetic moment is calculated in SI units as $\mu_{eff} / \mu_B = 798[(\chi_{mol} - \chi_{dia})T]^{1/2}$.

Computational methods

All calculations described in this paper were done using spin-unrestricted density functional theory as implemented in the GAUSSIAN 03 program, version D.02.[27] The B3LYP functional[28] was used throughout, in conjunction with the LANL2DZ basis set and associated effective core potential for Fe and Cl,[29] and Dunning's D95 basis set for C, N, O and H (856 basis functions in total).[30] The geometry of the Fe_8 cluster, $Fe_8(\mu_4\text{-}O)_4(\mu\text{-}pz)_{12}Cl_4$, was taken from our previously published paper[20], with no imposed symmetry constraints. Calculations on the broken-symmetry ($M_S = 0$) states were done using the converged high-spin ($M_S = 20$) density as an initial guess. Convergence to the required states with a local high-spin ($M_S = 5/2$) configuration at each Fe-center was then achieved in several steps using the guess=permute and guess=alter keywords.[31]

X-ray Crystallographic Data Collection and Refinement of the Structure

Suitable crystals for X-ray measurement for **1** and **4** were obtained by recrystallization of compounds from dichloromethane. For **2** and **3**, crystals of suitable quality were obtained directly from reactions similar to the ones described above. Crystals were selected from a

mixture of cluster and side products, which crystallize as the first solid fraction directly after synthesis. That fraction typically contains well developed crystals of **2** or **3** together with colorless crystals of triethylammonium chloride.

X-ray diffraction data, collected from a single crystals mounted atop glass fibers with a Siemens SMART 1K CCD diffractometer,[32a] were corrected for Lorentz and polarization effects. [32b] The structures were solved employing the SHELX-90[32c] program and refined by least-squares method on F^2, SHELXTL-93,[32d] incorporated in SHELXTL, Version 5.1.[32e] Crystallographic details for **1**, **2**, **3**, and **4** are summarized in Table 1.

Results and Discussion

The reactions of anhydrous FeX_3, X = Cl, Br, with pyrazole, or 4-substituted pyrazole, in CH_2Cl_2 under an inert atmosphere give bright red products, which consist of mixtures of $FeX_3(pz*H)_3$ and $[FeX_2(pz*H)_4][FeX_4]$.[33] Further addition of NEt_3 to that mixture (to deprotonate the pyrazole ligands) and exposure to air results in the formation of dark red octanuclear clusters **1** – **4**, which have been characterized in solution as well as in the solid state. During recrystallization of **2** and **3**, solvent molecules are trapped in interstitial cavities between the approximately spherical cluster molecules resulting in the overall formula $[Fe_8(\mu_4\text{-}O)_4(\mu\text{-}4\text{-}Cl\text{-}pz)_{12}Cl_4]\cdot 2CH_2Cl_2\cdot 1/2THF\cdot 4H_2O$ for **2** and $[Fe_8(\mu_4\text{-}O)_4(\mu\text{-}4\text{-}Me\text{-}pz)_{12}Cl_4]\cdot H_2O$ for **3**. The presence of solvent molecules in **2** was detected by ^1H-nmr and IR spectroscopies and supported by elemental analysis results, while the water molecule of **3** was identified during the crystal structure study. Slow water loss causes crystal decomposition of **3** with time; its elemental analysis was calculated for water-free sample.

X-Ray Crystallography

The crystal structures of **1** – **4** (Figure 1) consist of a Fe_4O_4-cubane encapsulated inside a shell of four $Fe(pz*)_3Cl$ units (the crystal structure of the hexane solvate of **1** has been previously communicated[20]). Bond lengths and angles for **1** – **4** are summarized in Table 2. While the inorganic $Fe_8(\mu_4\text{-}O)_4$ cores of **1-4** are tetrahedral, the pyrazole ligands are tilted out of the mirror plane positions, thus reducing the point group symmetry from T_d to T; the 4 C_3- and 3 C_2-axes of the T point group are running parallel to the $Cl\text{-}Fe_o\text{-}O\cdots Fe_c$ axes and through the centers of opposite Fe_2O_2 faces of the cubane, respectively. Within the Fe_4O_4 cubanes, the Fe-O bonds range from 2.03 to 2.07 Å, while the Fe-O-Fe and O-Fe-O angles vary from 96.5 to 99.0 and from 80.7 to 82.9°, respectively. The Fe_2O_2-faces of the cubane-cores deviate only slightly from planarity, in contrast to the Fe_2S_2-butterfly arrangement in Fe_4S_4-cubanes. Both, Fe-O and Fe-N bonds, are slightly shorter for the 5-coordinate outer Fe-atoms (Fe_o) compared to those of 6-coordinate cubane Fe-atoms (Fe_c). The introduction of an electron-withdrawing (Cl, **2**), or an electron-releasing (Me, **3**) substituent at the pyrazole 4-position, or the replacement of terminal chlorine by bromine ligands (**4**) have no significant effect on the structural parameters of the Fe_4O_4-cubanes, which remain practically invariant, in all four structures.

The $Fe_8(\mu_4\text{-}O)_4$ motif of **1** – **4** (Scheme 1) closely resembles the $Fe_8(\mu_4\text{-}O)_4$-units present in the all-ferric minerals ferrihydrite ($Fe_5HO_8\cdot 4H_2O$) and maghemite ($\gamma\text{-}Fe_2O_3$), but also in mixed-valent magnetite (Fe_3O_4).[34-36] The $Fe_c - O$ bond lengths of **1** – **4** are within the range for the corresponding bonds of maghemite and ferrihydrite, but shorter than those of magnetite, consistent with the mixed-valent nature of the latter (Table 3). The $Fe_c\cdots Fe_c$, as well as O-Fe_c-O and Fe_c-O-Fe_c angles of **1** - **4**, and the three minerals are also similar. Besides ferrihydrite, maghemite and magnetite, the $Fe_8(\mu_4\text{-}O)_4$ motif has also been found recently in the salicylaldoximate complex $Fe_8^{III}O_4(sao)_8(py)_4$ of S_4 symmetry, which contains only 6-coordinate Fe-atoms.[19] The irregular $Fe_4(\mu_4\text{-}O)_4$ cubane core of the latter complex has butterfly-distorted Fe_2O_2 faces with Fe_c-O bond lengths in the range of 1.990 – 2.231 Å.

The Ga-analogue of **1**, $Ga_8(\mu_4\text{-O})_4(\mu\text{-pz})_{12}Cl_4$, is also known.[37] As Ga^{III} and Fe^{III} have similar radii, the bond lengths and angles around the Ga-centers are quite similar to those around the Fe-centers of **1**.[38]

NMR data analysis

The solution ^{1}H-nmr spectra of **1**, **3** and **4** all show three broad, singlet, paramagnetically-shifted resonances (Table 4) assigned to the pyrazole 3-, 4-, and 5-positions and two resonances in the spectrum of the 4-Cl-pz complex **2** corresponding to the pyrazole 3- and 5-positions, consistent with their molecular formulae (Scheme 1). The magnetic equivalence of twelve pyrazole rings confirms the *T* molecular symmetry of all four complexes in solution. Complexes **1** and **4** differ only in their terminal halogen ligands. Their corresponding ^{1}H-NMR spectra differ most significantly in their upfield resonances, 3.5 ppm for **1** and 1.0 ppm for **4**, on the basis of which we tentatively assign them to the proximal ^{5}H (position-3 is defined as the one closer to the Fe_4O_4-cubane, while position-5 is the one closer to a outer Fe-centers, Scheme 1). By analogy, the upfield resonances of **2** and **3** (8.6, and 3.8 ppm) are also assigned to the ^{5}H atoms. For **3**, the peak area integration clearly identifies the methyl-group downfield resonance at 27.7 ppm. Similarly, the downfield resonances of **1** and **4** (42.2 and 42.9 ppm) are also assigned to the ^{4}H atoms. This leaves the midfield resonances of all four complexes assigned to their ^{3}H atoms. Comparison of ^{1}H-NMR spectra for **1** and **2** shows the influence of Cl-atom in 4-position of pyrazole; the ^{3}H and ^{5}H of **2** are shifted approximately 3 and 5 ppm downfield.

Vibrational spectroscopy

The IR spectra of **1** - **4** (Supplementary Information, S1) consist of absorptions in the 1600 – 500 cm^{-1} range assigned to pyrazole vibrations. An addition absorption assigned to a Fe-O stretch is observed at 475 cm^{-1} (**1**), 478 cm^{-1} (**2**), 476 cm^{-1} (**3**) and 475 cm^{-1} (**4**). In ^{18}O-labelled **2**, this band shifts to 466 cm^{-1}, confirming its assignment. An absorption assigned to a Fe-O stretch, observed in the Raman spectrum of **2** at 441 cm^{-1}, shifts to 428 cm^{-1} in the ^{18}O-labelled sample (Supplementary Information, S2).

Electrochemistry

The electrochemical properties of complexes **2** – **4**, as determined by cyclic voltammetry, are similar to those already reported for **1**.[20] All four complexes show four reversible one-electron processes that reduce the neutral complexes to their corresponding mono-, di-, tri-, and tetraanions (Figure 2). Inspection of the $E_{1/2}$-values of complexes **1** - **4** (Table 5) shows that substitution, both at the peripheral μ-pyrazole 4-positions as well as of the terminal halide ligands, influences the redox properties of the complex. The introduction of twelve electron-withdrawing chlorine substituents causes an anodic shift of $0.01 - 0.20$ V of the $E_{1/2}$ values of **2** compared to **1**, while the introduction of twelve electron-releasing methyl group substituents causes a cathodic shift of $0.10 – 0.15$ V to those of **3**. The exchange of terminal Cl- for Br-ligands in **4**, on the other hand, brings about an anodic shift of $0.10 – 0.29$ V. The fact that the two different types of substitution cause $E_{1/2}$ shifts of the same magnitude argues for the redox-active centers of the Fe_8 complexes being remote from both substitution sites, e.g., the redox activity is confined to the six-coordinate centers of the encapsulated Fe_4O_4-cubane, not the four outer five-coordinate Fe-centers, which are directly connected to the terminal halide ligands. The rich redox chemistry of complexes **1** – **4** distinguishes them from other known Fe_4O_4-complexes for which no reversible electrochemistry has been reported to date. We attribute this to the protection afforded by the outer, inert shell, consisting of four Fe (μ-pz)$_3$-units to the redox-active Fe_4O_4-core of **1** – **4**.

The separation measured here between the first and fourth redox process of each Fe_8 complex, $\Delta E_{1-4} = 0.95$ V (**1**), 0.83 V (**2** and **4**) and 0.97 V (**3**), is much larger than the theoretical

$\Delta E_{1-4} = 0.0712$ V separation in a system of four non-interacting redox centers.[39] Whilst the degree of electronic communication among Fe-centers cannot be determined from the separation of $E_{1/2}$ values (solvation and ion-pairing effects can significantly influence $E_{1/2}$ values), the $\Delta E_{n-(n+1)}$ values of **1 – 4** indicate some degree of valence delocalization. A qualitative comparison between isovalent $\Delta E_{n-(n+1)}$ values of Fe_4O_4 and Fe_4S_4 cubanes shows a larger separation between consecutive redox processes in the latter, evidence of a higher degree of charge delocalization in the iron-sulfur clusters. The narrow ΔE_{1-4} separation of 0.83 – 0.97 V found here for Fe_4O_4 cubanes means that they can shuttle four electrons across a narrower redox potential window than the corresponding Fe_4S_4 cubanes; Fe_4O_4 cubanes are more efficient electron-transfer agents. As electron acceptors, the Fe_8 complexes **1 – 4** are more efficient than C_{60} for which the first four redox processes are separated by 0.43 – 0.53 V, giving a ΔE_{1-4} of 1.41 V.[40]

Analysis of Magnetic Data of 1

The effective magnetic moment, μ_{eff}, at $T = 300$ K is 7.0 μ_B and on cooling this gradually descends to 0.12 μ_B at $T = 2.0$ K (Figure 3). The value at room temperature is much smaller than expected for eight uncoupled Fe^{III} centers with g = 2.0 ($\mu_{eff} = 16.7$ μ_B), and the decrease of the magnetic susceptibility upon cooling confirms the presence of strong antiferromagnetic exchange interaction in **1**. The inverse susceptibility is non-linear and as a result of these exchange interactions which result in unequal population of energy levels.

In order to interpret the magnetic properties, the following spin Hamiltonian was postulated:

$$\widehat{H} = -J_1 \sum_{i=1}^{4}\sum_{j>i}^{4} S_i \cdot S_j - J_2 \sum_{k=1,2,3} S_5 \cdot S_k - J_2 \sum_{k=1,2,4} S_6 \cdot S_k - J_2 \sum_{k=2,3,4} S_7 \cdot S_k$$
$$-J_2 \sum_{k=1,3,4} S_8 \cdot S_k + \mu_B \sum_{i=1}^{8} S_i \cdot g_i \cdot B$$

(1)

where J_1 represents the isotropic exchange interactions in the $Fe^{III}_4O_4$-cubane core mediated only through μ_4-O bridges, J_2 represents the isotropic exchange interactions between each apical Fe^{III} center and the triangular base of the inner tetrahedron to which it lies closest, mediated through μ_4-O and μ-pz bridges (Scheme 2) and the last term is the Zeeman term. We have ignored the coupling between the outer Fe centers, which is expected to be small due to the large internuclear separation.

The exchange coupling of eight Fe^{III} centers, each with the local spin $S_i = 5/2$, leads to $(2S_i + 1)^8 = 6^8 = 1\,679\,616$ magnetic states with total spin ranging from $S = 0$ to $S = 20$. Unfortunately, the postulated spin Hamiltonian is not symmetric and it is not possible to obtain an analytical formula for energy levels. Moreover, it is not feasible to efficiently diagonalize such large interaction matrices. To reduce the dimensions of the matrices, we have focused on the total spin symmetry principle (TSSP) for which the conditions (*g*-factors equal for all magnetic centers and no non-isotropic terms present) are fulfilled.[41] In order to take advantage of TSSP approach, it is necessary to calculate energy values in the coupled basis set labeled as $|\alpha SM\rangle$ using irreducible tensor operators,[42] where α stands for the intermediate quantum numbers denoting the coupling path. First, only the isotropic exchange terms are involved and the whole matrix is factorized into the blocks according to the final spin quantum number S. As a result, the energies in zero magnetic field are obtained. The largest dimension of the sub-matrix is 16576 for $S = 5$ (Supplementary Information, S3). Consequently, the energy levels in non-zero magnetic field are calculated as $E_i(\alpha SM) = E_{0,i}(\alpha S) + \mu_B g BM$. Nowadays, this approach is feasible on modern computers, but it takes a few days to calculate the whole energy spectrum. Obviously, this procedure is not suitable for fitting of the magnetic data and further reduction of the dimensions of the matrices is needed.

To solve this problem, the spin permutational symmetry (SPS) of the spin Hamiltonian was applied[41] and the energy levels were classified (Figure S1) according to the irreducible representation of the D_2 point group (D_2 is a subgroup of the local T_d symmetric Fe_8O_4 core). Numerically efficient use of the SPS approach demands a coupling scheme, which is left invariant under the symmetry operations of the point group. This condition is fulfilled for $\mathbf{S}_{12} = \mathbf{S}_1 + \mathbf{S}_2$, $\mathbf{S}_{34} = \mathbf{S}_3 + \mathbf{S}_4$, $\mathbf{S}_{56} = \mathbf{S}_5 + \mathbf{S}_6$, $\mathbf{S}_{78} = \mathbf{S}_7 + \mathbf{S}_8$, $\mathbf{S}_{1234} = \mathbf{S}_{12} + \mathbf{S}_{34}$, $\mathbf{S}_{5678} = \mathbf{S}_{56} + \mathbf{S}_{78}$, $\mathbf{S} = \mathbf{S}_{1234} + \mathbf{S}_{5678}$. As a result, the each exchange matrix for final spin S is further factorized in relation to the irreducible representation of D_2 point group. Now, the largest matrix has the dimension of 4201 for $S = 4$, $\Gamma = A_1$ and calculation of the whole energy spectrum is much faster (Supplementary Information, S3).

Having the energy levels labeled as $E_i(\alpha SM, \Gamma_j) = E_{0,i}(\alpha S, \Gamma_j) + \mu_B g BM$, the molar magnetization can be easily calculated as

$$M_{\mathrm{mol}} = N_A \mu_B g B \frac{\sum_i M \exp\left[-E_i\left(\alpha S\, M, \Gamma_j\right)/kT\right]}{\sum_i \exp\left[-E_i\left(\alpha S\, M, \Gamma_j\right)/kT\right]}$$

(2)

Fitting the experimental magnetization to this expression resulted in the following set of parameters: $J_1/hc = -2.1$ cm^{-1}, $J_2/hc = -50.6$ cm^{-1} with fixed $g = 2.0$. The fitting procedure was rather insensitive to the (small) value and sign of the coupling constant J_1. The grid of error functional R,[43] for varying J_1 and J_2 parameters was calculated to confirm that the solution is the global minima (Supplementary Information, S3). Also, the standard deviations were calculated for fitted parameters with 95% probability and resulted in $J_1/hc = -2.1 \pm 2.6$ cm^{-1} and $J_2/hc = -50.55 \pm 0.24$ cm^{-1}.

The large negative value of J_2 indicates significant antiferromagnetic coupling between the inner and outer magnetic centers and is consistent with the magnetic measurements. The magnetic interaction in the Fe_4O_4 cubane core is weak and most probably antiferromagnetic in nature, although the possibility of a very small ferromagnetic interaction cannot be excluded on the basis of the magnetic properties.

The reconstructed energy levels in zero magnetic field as a function of final spin S are shown in Figure 4. The ground state is $S = 0$, and it is evident that the rotational band is retained for the bottom level of each spin, which is expected for antiferromagnetic coupled clusters.[44] Obviously, only a very limited part of the energy spectrum is thermally populated, explaining the deviation of magnetic susceptibility from the Curie-Weiss law.

Electronic structure of 1

In order to shed further light on the magnetic interactions in the parent cluster, $Fe_8(\mu_4\text{-}O)_4(\mu\text{-}pz)_{12}Cl_4$, we have explored its electronic structure using spin-unrestricted density functional theory (B3LYP functional). Using the crystallographically determined geometry, we have computed the energies of three distinct electronic configurations (Scheme 2), differing in the relative orientations of the spins vectors. The first of these, the high-spin state (HS), has $M_S = 20$, while the two broken-symmetry states, BS1 and BS2, have $M_S = 0$.

HS, $|5/2\rangle|5/2\rangle|5/2\rangle|5/2\rangle|5/2\rangle|5/2\rangle|5/2\rangle|5/2\rangle$

BS1, $|5/2\rangle|5/2\rangle|5/2\rangle|5/2\rangle|-5/2\rangle|-5/2\rangle|-5/2\rangle|-5/2\rangle$

BS2, $|5/2\rangle|5/2\rangle|-5/2\rangle|-5/2\rangle|-5/2\rangle|-5/2\rangle|5/2\rangle|5/2\rangle$

In **BS1**, the spin vectors on the inner core are aligned parallel to each other (ferromagnetic), but antiparallel to those on the outer iron centres. In **BS2** in contrast, the Fe_4O_4 core is subdivided into a 'dimer-of-dimers' structure, with the spins on the upper half aligned antiparallel to those on the lower half (similar models of electronic structure have been used to describe the antiferromagnetic coupling in Fe_4S_4 cubanes).[45] The outer tetrahedron is similarly divided into upper and lower halves, with the spin vectors aligned antiparallel to those in the Fe_4O_4 core.

Applying the Heisenberg spin Hamiltonian:

$$\widehat{H} = -J_1 \sum_{i=1}^{4} \sum_{j>i}^{4} S_i \cdot S_j - J_2 \sum_{k=1,2,3} S_5 \cdot S_k - J_2 \sum_{k=1,2,4} S_6 \cdot S_k - J_2 \sum_{k=2,3,4} S_7 \cdot S_k - J_2 \sum_{k=1,3,4} S_8 \cdot S_k$$

(3)

to each of these three single determinant wavefunctions gives the following expressions for energies:

$$E(HS) = -\frac{150}{4} J_1 - \frac{300}{4} J_2, E(BS1) = -\frac{150}{4} J_1 + \frac{300}{4} J_2, E(BS2) = +\frac{50}{4} J_1 + \frac{100}{4} J_2$$

From which the expressions for J_1 and J_2 can be derived:

$$J_2 = \frac{E(BS1) - E(HS)}{150} \quad \text{and} \quad J_1 = \frac{3E(BS2) - 2E(BS1) - E(HS)}{150}$$

The computed total energies, and net spin densities at each iron center are summarized in Table 6, along with expectation values of the square of the total spin operator, $<S^2>$. Spin densities of 4.0-4.2 are typical of high-spin Fe^{III} centers, while the values of $<S^2>$ are close to the ideal values for ferromagnetic ($<S^2> = 420$) and broken-symmetry ($<S^2> = 20$) states arising from the coupling between eight $S = 5/2$ single ions.

The resulting calculated values of $J_1/hc = -6.3$ cm^{-1} and $J_2/hc = -52.8$ cm^{-1} are in excellent agreement with the experimental values of -2.1 cm^{-1} and -50.6 cm^{-1}, respectively, and confirm the dominance of antiferromagnetic coupling between the inner and outer Fe centres, mediated by the μ_4-O bridges. The much stronger antiferromagnetic coupling between the inner and outer iron centres is related to the larger angles subtended at the bridging oxide ligands (119°), as a result of which the Fe_c-O-Fe_o superexchange pathway is more efficient than Fe_c-O-Fe_c, where the angles are closer to 90° (98°). The partial delocalization of the Fe_o d_{z^2} electron onto the Fe_c center is apparent in the contour plot of the HOMO of BS2 (shown Figure 5). We note that Murrie and co-workers have reported similar antiferromagnetism in their $[Fe_8^{III}O_4(sao)_8(py)_4]\cdot4py$ system, and proposed that the dominant exchange pathway is also mediated by the μ_4-O ligands.[19]

The localization of the molecular orbitals around the frontier region also sheds some light on the observed electrochemical properties. In each case (HS, BS1 and BS2), the lowest vacant orbitals are largely localized on the inner Fe_4O_4 core (HOMO and LUMO are shown for the BS2 state in Figure 5), consistent with our proposal that this is the site of the four reduction processes. There is, however, some significant delocalization onto the outer Fe centers, Fe_o, which would lead to a buffering of the electronic effects of successive reductions, as proposed by Lippard *et al.*[15]

Mössbauer spectroscopy

At zero magnetic field the Mössbauer spectra of **1** consist of two quadrupole doublets in the 4.2 - 300 K temperature range. The zero field spectrum recorded at 4.2 K is shown in Figure

6. The deconvolution of the zero field spectra may be carried out assuming two different models with either two "nested" (Fig. 6) or two "crossed" doublets (Supplementary Information, S4). The parameters obtained by the two methods are listed in Table 7. For either model, it is ascertained that the isomer shift values in the whole temperature range fall in the range of high spin ferric ions in octahedral environment with N/O donors.[#] Moreover, for both models, the site with the lower isomer shift value (A, $\delta = 0.37$ and 0.32 mm s^{-1} at 4.2 K) is characterized by the largest quadrupole splitting (B, $|\Delta E_Q| = 0.68$ and 0.57 mm s^{-1}).

The Mössbauer parameter values strongly indicate that site A corresponds to the five-coordinate peripheral ions, Fe_o, whereas site B corresponds to the six-coordinate cubane ferric ions, Fe_c.[46] The decrease of the isomer shift upon decrease of coordination number is associated with a decrease of the bond length, as it appears for the peripheral ferric ions with bond lengths slightly shorter than those of the cubane. The symmetry of the peripheral Fe_o-centers is lower than that of the cubane ones, Fe_c, and this is reflected in the larger ΔE_Q value of site A in both models.[47] Similar δ-values to those of Fe_c of **1** with *fac*-O$_3$N$_3$ coordination have been observed in the low temperature spectra of a mononuclear complex with *cis*-O$_2$N$_4$ coordination ($\delta = 0.44$ mm s^{-1} at 80 K), a dinuclear complex containing a Fe$_2$O$_2$-core with O$_6$ and O$_5$N coordination ($\delta = 0.45$ mm s^{-1} at 4.2 K) and horse spleen ferritin ($\delta = 0.45$ mm s^{-1} at 100 K).[48-50] Furthermore, the structural similarity of **1** to the minerals ferrihydrite and maghemite also holds true for their Mössbauer isomer shifts (Table 3).[51,52]

From the analysis of the magnetic susceptibility measurements for **1** a diamagnetic ($S = 0$) ground state is inferred with an $S = 1$ excited state ~39 cm^{-1} higher in energy. An isolated ground state with $S = 0$ is further supported by the Mössbauer spectra. In Figure 6 we show a spectrum recorded at 4.2 K in the presence of an external magnetic field of 6 T applied perpendicular to the γ-rays.

In an exchanged coupled system the local magnetic field induced on each ferric site of the cluster is given by:

$$B_{tot} = B_{ext} + B_{int} \qquad (4)$$

where $\mathbf{B_{ext}}$ is the applied magnetic field and $\mathbf{B_{int}} = -a_i \langle \mathbf{S_i} \rangle / g_n \beta_n$.

a_i is the intrinsic hyperfine tensor for a ferric ion; $\langle \mathbf{S_i} \rangle$ is the spin expectation value for each ferric ion and critically depends on the total spin S of each multiplet of the exchange coupled system and the exchange coupling scheme. For states with total spin $S = 0$, $\langle \mathbf{S_i} \rangle = 0$. In such cases each ferric ion nucleus will experience only the external field $\mathbf{B_{ext}}$. The magnetically perturbed spectrum of Figure 6 can be readily simulated assuming two sites with $\mathbf{B_{int}} = 0$ (within experimental error) indicating that the ground state of the cluster is diamagnetic, well isolated from states with nonzero total spin. We have fitted the magnetically perturbed spectrum assuming both models (nested or crossed) and better results were obtained assuming the nested one (shown in Figure 6). Finally, the analysis of the magnetically perturbed spectra allowed for the estimation of the asymmetry parameter η of the Electric Field Gradient tensor (EFG) along with the determination of the sign of the quadrupole splitting. For both deconvolution models the quadrupole splitting is found to be negative.

Conclusions

The crystal structures of the octanuclear complexes **1**-**4** show that the 3- and 5-position of pyrazole ligands are sterically hindered in these materials, while the 4-position radiate

---

[#]The decrease in the values of isomer shifts from 4.2 K to 293 K is attributed to a second order Doppler effect.[46]

unhindered out of the approximately spherical structure. Further property tuning in the family of $Fe_8(\mu_4\text{-}O)_4$-containing compounds can be achieved by the introduction of appropriate substituents at the pyrazole 4-position, as has been shown here for the redox properties of **1** – **3**.

There have been only a few examples of polynuclear Fe^{III} clusters of which the magnetic properties have been thoroughly analyzed to date.[53] The main theoretical complication lies in a very high number of spin states; this problem can be solved gracefully by using symmetry of the spin Hamiltonian, which was successfully presented in the article. Analysis of the temperature dependence of the magnetic susceptibility indicates the presence of strong antiferromagnetic coupling between the inner and outer Fe centers, with rather weaker coupling within the Fe_4O_4 core. The computed electronic structure of the cluster confirms the presence of highly localized high-spin Fe^{III} centers, and also the dominance of the superexchange pathway between core and outer iron centers, mediated by the μ_4-O bridge. Furthermore, although the lowest lying vacant orbitals are found to be largely localized on the core irons, significant delocalization onto the outer metal centers will buffer the redox events to some extent, possibly accounting for the very narrow window over which the four one-electron reduction steps occur.

The $M_8(\mu_4\text{-}O)_4$-motif is common in metal complexes, as well as in minerals. Complexes in which the $M_8(\mu_4\text{-}O)_4$-core is supported by twelve bridging ligands are known in both carboxylate (M = Cr,[54] Co,[55] V/Zn,[56] Fe[19]) and pyrazolate systems (M = Ga,[30] Fe – Scheme 1). The Fe^{III}-minerals maghemite and ferrihydrite and the $Fe^{III/II}$ magnetite contain $Fe_8(\mu_4\text{-}O)_4$-units. In the extended structures of all three of those minerals, the six-coordinate Fe_c-vertices are shared between two consecutive cubanes, while the Fe_o are *tetrahedrally* coordinated by four μ_4-O atoms of four cubane units (while the Fe_o-centers of **1** – **4** are *trigonal bipyramidal*). In contrast, in the structures of **1** – **4** the twelve pyrazole bridges and the four terminal halogen atoms block all the remaining coordination sites of the $Fe_8(\mu_4\text{-}O)_4$ core, arresting its polymeric growth. The structural similarity between the iron-oxide core of ferritin and ferrihydrite has been known for quite some time.[57] The further similarity between ferrihydrite and the core of complexes **1** – **4** described here, implies that the latter are models of the building units of ferritin.

The present study has established the structural, spectroscopic, electrochemical, magnetic properties and electronic structure of the all-ferric Fe_4O_4-cubane, providing the respective "fingerprints", which may allow the recognition of this species in Nature, if indeed it exists. Ferrihydrite, maghemite and magnetite are possible sources from which intact $Fe_8(\mu_4\text{-}O)_4$ units might be extruded by proteins. An electron transfer protein based on a redox-active Fe_4O_4-cubane may of course exist in an all-ferric, or any of the four reduced mixed-valent or all-ferrous states. The full characterization of pyrazolate complexes containing redox-modified Fe_4O_4-cubanes, as well as a detailed investigation of the evolution of the electronic structure on reduction, are currently underway in our laboratories.

Supplementary Material

Refer to Web version on PubMed Central for supplementary material.

Acknowledgements

References

1. a Beinert H, Holm RH, Münck E. Science 1997;277:653. [PubMed: 9235882] b George DG, Hunt LT, Yeh LS, Baker WC. J Mol Evol 1985;22:20. [PubMed: 3932661] c Zhou ZH, Adams MWW. Biochemistry 1997;36:10892. [PubMed: 9283079] d Ma K, Hutchins A, Sung SJS, Adams MWW. Proc Natl Acad Sci USA 1997;94:9608. [PubMed: 9275170] e Kisker C, Schindelin H, Rees DC. Annu Rev Biochem 1997;66:233. [PubMed: 9242907] f Tainer JA, Thayer MM, Cunningham RP. Curr Opin Struct Biol 1995;5:20. [PubMed: 7773744] g Pereira IAC, Romao CV, Xavier AV, LeGall J, Teixeira MJ. J Biol Inorg Chem 1998;3:494. h Peters JW, Lanzilotta WN, Lemon BJ, Seefeldt LC. Science 1998;282:1853. [PubMed: 9836629] i Nicolet Y, Piras C, Legrand P, Hatchikian EC, Fontecilla Camps JC. Structure 1999;7:13. [PubMed: 10368269] j Breiter DR, Meyer TE, Rayment I, Holden HM. J Biol Chem 1991;266:18660. [PubMed: 1917989] k Kim J, Rees DC. Biochemistry 1994;33:389. [PubMed: 8286368] l Cammack R, Fernandez VM, Hatchikia EC. Methods Enzymol 1994;243:43. m Crane BR, Getzoff ED. Curr Opin Struct Biol 1996;6:744. [PubMed: 8994874]

2. Rao PV, Holm RH. Chem Rev 2004;104:527. [PubMed: 14871134]

3. a Arendsen AF, Hadden J, Card G, McAlpine AS, Bailey S, Zaitsev V, Duke EHM, Lindley PF, Kröckel M, Trautwein AX, Feiters MC, Charnock JM, Garner CD, Marritt SJ, Thompson MK, Kooter IM, Johnson MK, van den Berg WAM, van Dongen WMAM, Hagen WR. J Biol Inorg Chem 1998;3:81. b van den Berg WAM, Hagen WR, van Dongen WMAM. Eur J Biochem 2000;267:666. [PubMed: 10651802]

4. a Wolfe MT, Heo J, Gararelli JS, Ludden PW. J Bacteriol 2002:5898. [PubMed: 12374823] b Cabello P, Pino C, Olmos-Mira MF, Castillo F, Roldan MD, Moreno-Vivian C. J Biol Chem 2004;279:45485. [PubMed: 15322098]

5. Dobbek H, Svetlitchnyi V, Gremer L, Huber R, Meyer O. Science 2001;293:1281. [PubMed: 11509720]

6. Fank P, De Tomaso A, Hedman B, Hodgson KO. Inorg Chem 2006;45:3920. [PubMed: 16676950]

7. a Wallar BJ, Lipscomb JD. Chem Rev 1996;96:2625. [PubMed: 11848839] b Klabunde T, Krebs B. Struct Bond 1997;89:177. c Lange SJ, Que L Jr. Curr Opin Chem Biol 1998;2:159. [PubMed: 9667935] d Westerheide L, Pascaly M, Krebs B. Curr Opin Chem Biol 2000;4:235. [PubMed: 10742188]and references therein

8. Ford GC, Harrison PM, Rice DW, Smith JMA, Treffry A, White JL, Yariv J. Phil Trans R Soc London 1984;304:551. [PubMed: 6142491]B

9. Shoner SC, Power PP. Inorg Chem 1992;31:1001.

10. Taft KL, Caneschi A, Pence LE, Delfs CD, Papaefthymiou GC, Lippard SJ. J Am Chem Soc 1993;115:11753.

11. Taft L, Papaefthymiou GC, Lippard SJ. Science 1993;259:1302. [PubMed: 8446898]

12. Taft KL, Papaefthymiou GC, Lippard SJ. Inorg Chem 1994;33:1510.

13. Dell'Amico DB, Boschi D, Calderazo F, Ianelli S, Labella L, Marchetti, Pelizzi G, Quadrelli EGF. Inorg Chim Acta 2000;300-302:882.

14. a Oshio H, Hoshino N, Ito T. J Am Chem Soc 2000;122:12602. b Oshio H, Hoshino N, Ito T, Nakano M. J Am Chem Soc 2004;126:8805. [PubMed: 15250734]

15. Lee D, Sorace L, Caneschi A, Lippard SJ. Inorg Chem 2001;40:6774. [PubMed: 11735490]

16. Clemente-Juan JM, Mackiewicz C, Verelst M, Dahan F, Bousseksou A, Sanakis Y, Tuchagues JP. Inorg Chem 2002;41:1478. [PubMed: 11896717]

17. Abrahams BF, Hudson TA, Robson R. J Am Chem Soc 2004;126:8624. [PubMed: 15250694]

18. Hudson TA, Berry KJ, Moubaraki B, Murray K, Robson R. Inorg Chem 2006;45:3549. [PubMed: 16634585]

19. Gass IA, Milios CJ, Whittaker AG, Fabiani FPA, Parsons S, Murrie M, Perlepes SP, Brechin EK. Inorg Chem 2006;45:5281. [PubMed: 16813389]

20. Raptis RG, Georgakaki IP, Hockless DCR. Angew Chem Int Ed 1999;38:1632.

21. a Stephens PJ, Jollie DR, Warshel A. Chem Rev 1996;96:2491. [PubMed: 11848834] b Zanello PA. Coord Chem Rev 1988;87:1. c Zanello P. Coord Chem Rev 1988;83:199.

22. Martin W, Russell MJ. Phil Trans R Soc Lond B 2003;358:59. [PubMed: 12594918]

23. a Xiao ZG, Gardner AR, Cross M, Maes EM, Czernuszewicz RS, Sola M, Wedd AG. J Biol Inorg Chem 2001;6:638. [PubMed: 11472027] b Dilg AWE, Capozzi F, Mentler M, Iakovleva O, Luchinat C, Bertini I, Parak FG. J Biol Inorg Chem 2001;6:232. [PubMed: 11315559] c Xiao Z, Lavery MJ, Ayhan M, Scrofani SDB, Wilce MCJ, Guss JM, Tregloan PA, Goerge GN, Wedd AG. J Am Chem Soc 1998;120:4135.

24. Ehlert MK, Rettig SJ, Storr A, Thompson RC, Trotter J. Can J Chem 1991;69:432.

25. Perrin, DD.; Armarego, WLF.; Perrin, DR. Purification of Laboratory Chemicals. 2nd. Pergamon Press; 1987.

26. König, E. Landolt-Börstein, Neue Serie. 2. Springer; Berlin: 1966. p. 1-16.

27. FrischMJGaussian 03, Revision D.02Gaussian, Inc.Wallingford, CT2004Full reference is given in the supporting information, S5.

28. a Becke AD. J Chem Phys 1993;98:5648. b Lee C, Yang W, Parr RG. Phys Rev B 1988;37:785.Parr, RG.; Yang, W. Density Functional Theory of Atoms and Molecules. Oxford University Press; New York: 1989.

29. a Hay PJ, Wadt WR. J Chem Phys 1985;82:270. b Wadt WR, Hay PJ. J Chem Phys 1985;82:284.

30. a Dunning TH Jr. J Chem Phys 1970;53:2823–2833.Dunning, TH., Jr; Hay, PJ. Modern Theoretical Chemistry. Schaefer, HF., III, editor. 3. Plenum; New York: 1976. p. 1-28.

31. http://www.gaussian.com

32. SMART-NT Software Reference Manual, version 5.059. Bruker AXS, Inc.; Madison, WI: 1998. SAINT+ Software Reference Manual, version 6.02. Bruker AXS, Inc.; Madison, WI: 1999. Sheldrick, GM. SHELXS-90, Program for the Solution of Crystal Structure. University of Göttingen; Germany: 1986. Sheldrick, GM. SHELXL-97, Program for the Refinement of Crystal Structure. University of Göttingen; Germany: 1997. SHELXTL-NT Software Reference Manual, version 5.1. Bruker AXS, Inc.; Madison, WI: 1998.

33. Piñero, D.; Raptis, R. G. unpublished results.

34. Michel FM, Ehm L, Antao SM, Lee PL, Chupas PJ, Liu G, Strongin DR, Schoonen MAA, Phillips BL, Parise JB. Science 2007;316:1726. [PubMed: 17525301]

35. a Greaves C. J Solid State Chem 1983;49:325. b Sinha HP, Sinha APB. Z Anorg Allg Chem 1958;293:228.

36. Fleet MF. Acta Crystallogr 1981;B37:917.

37. Capparelli MV, Hodge P, Piggott B. Chem Commun 1997:937.

38. Shannon RD. Acta Crystallogr 1976;A32:751.

39. Flanagan JB, Margel S, Bard AJ, Anson FC. J Am Chem Soc 1978;100:4248.

40. a Xie Q, Pérez-Cordero E, Echegoyen L. J Am Chem Soc 1992;114:3978. b Ohsawa Y, Saji T. J Chem Soc Chem Commun 1992:781.

41. Waldmann O. Phys Rev B 2000;61:6138.

42. Boča, R. Theoretical Foundations of Molecular Magnetism. Elsevier; Amsterdam: 1999.

43. The error functional is defined as $R = 100 \left/ N \times \sum_{i}^{N} \left(1 - \mu_{eff,i}^{c} \left/ \mu_{eff,i}^{o}\right.\right)\right.$, where $\mu_{eff,i}^{c}$ is calculated effective moment, $\mu_{eff,i}^{o}$, is observed effective moment and N is number of experimental points.

44. Schnack J, Luban M. Phys Rev 2001;B63:014418.

45. a Noodleman L, Case DA. Adv Inorg Chem 1992;38:423. b Aizman A, Case DA. J Am Chem Soc 1982;104:3269. c Noodleman L, Peng CY, Case DA, Mouesca JM. Coord Chem Rev 1995;144:199.

46. Greenwood, NN.; Gibb, TC. Mössbauer Spectroscopy. Chapman and Hall Ltd; London: 1971.

47. Bill E, Krebs C, Winter M, Gerdan M, Trautwein AX, Flörke U, Haupt HJ, Chaudhuri P. Chem Eur J 1997;3:193.

48. Benisvy L, Halut S, Donnadieu B, Tuchagues JP, Chottard JC, Li Y. Inorg Chem 2006;45:2403. [PubMed: 16529458]

49. Yoon S, Lippard SJ. J Am Chem Soc 2004;126:2666. [PubMed: 14995160]

50. Watt GD, Frankel RB, Papaefthymiou GC. Proc Nat Acad Sci USA 1985;82:3640. [PubMed: 3858840]

51. Murad E, Bowen LH, Long GL, Quin TG. Clay Minerals 1988;23:161.

52. Annersten H, Hafner SS. Z Krist 1973;137:321.

53. a Waldmann O, Koch R, Schromm S, Schülein J, Müller P, Bernt I, Saalfrank RW, Hampel F, Balthes E. Inorg Chem 2001;40:2986. [PubMed: 11399165] b Mukhin A, Gorshunov B, Dressel M, Sangregorio C, Gatteschi D. Phys Rev B 2001;63 c Barra L, Caneschi A, Cornia A, de Biani F, Gatteschi D, Sangregorio C, Sessoli R, Sorace L. J Am Chem Soc 1999;121:5302. d Barra AL, Bencini F, Caneschi A, Gatteschi D, Paulsen C, Sangregorio C, Sessoli R, Sorace L. Chem Phys Chem 2001;2:523. e Benelli C, Cano J, Journaux Y, Sessoli R, Solan GA, Winpenny REP. Inorg Chem 2001;40:188. [PubMed: 11170519] f Gatteschi D, Caneschi A, Sessoli R, Cornia A. Chem Soc Rev 1996;25:101. g Delfs C, Gatteschi D, Pardi L, Sessoli R, Wieghardt K, Hanke D. Inorg Chem 1993;32:3099.

54. Atkinson IM, Benelli C, Murrie M, Parsons S, Winpenny REP. Chem Commun 1999:285.

55. Dimitrou K, Sun JS, Folting K, Christou G. Inorg Chem 1995;34:4160.

56. Cotton FA, Duraj SA, Roth WJ. Inorg Chem 1984;23:4042.

57. Ford GC, Harrison PM, Rice DW, Smith JMA, Treffry A, White JLJ, Yariv J. J Phil Trans R Soc (London) 1984;B304:551.
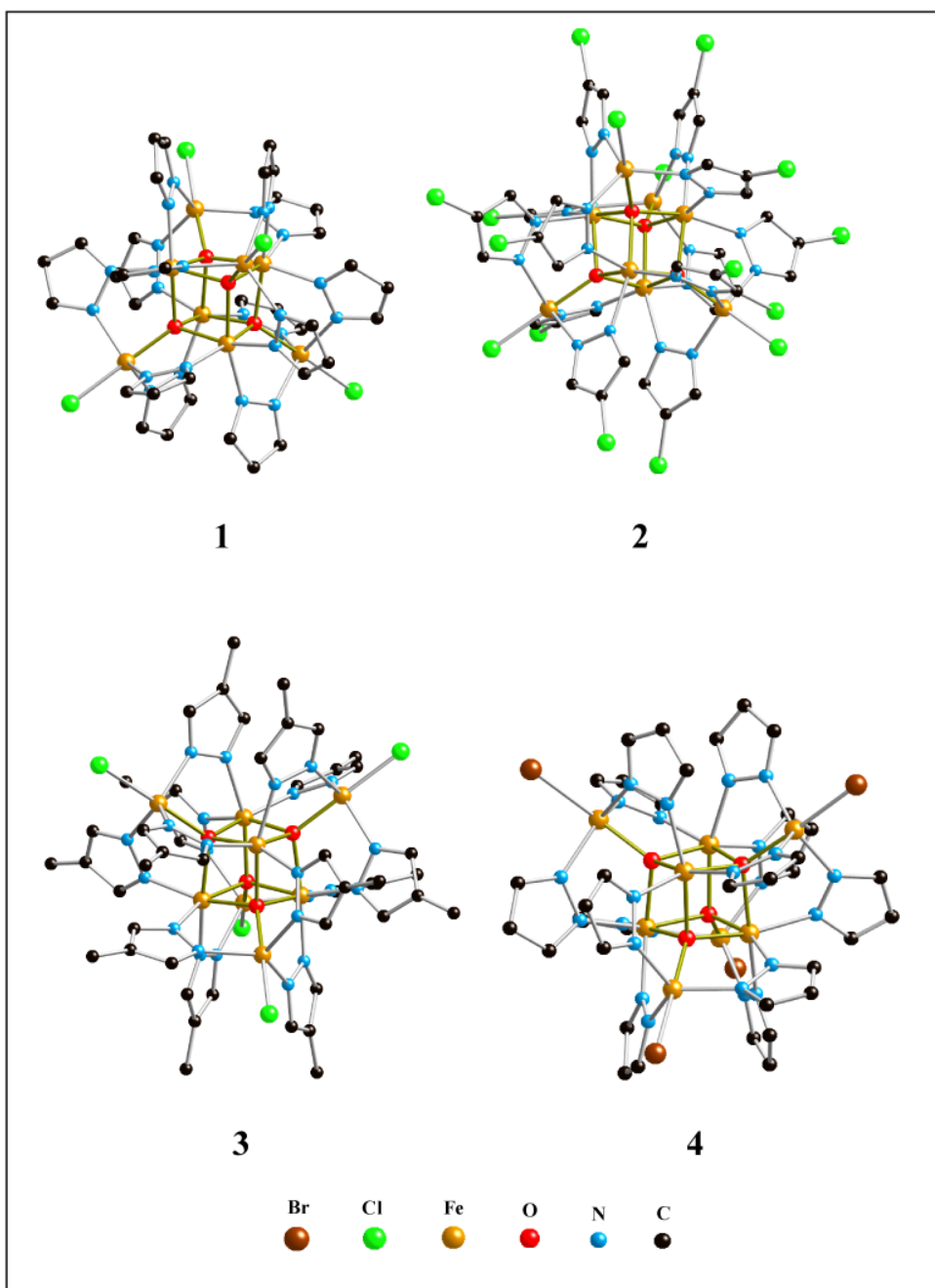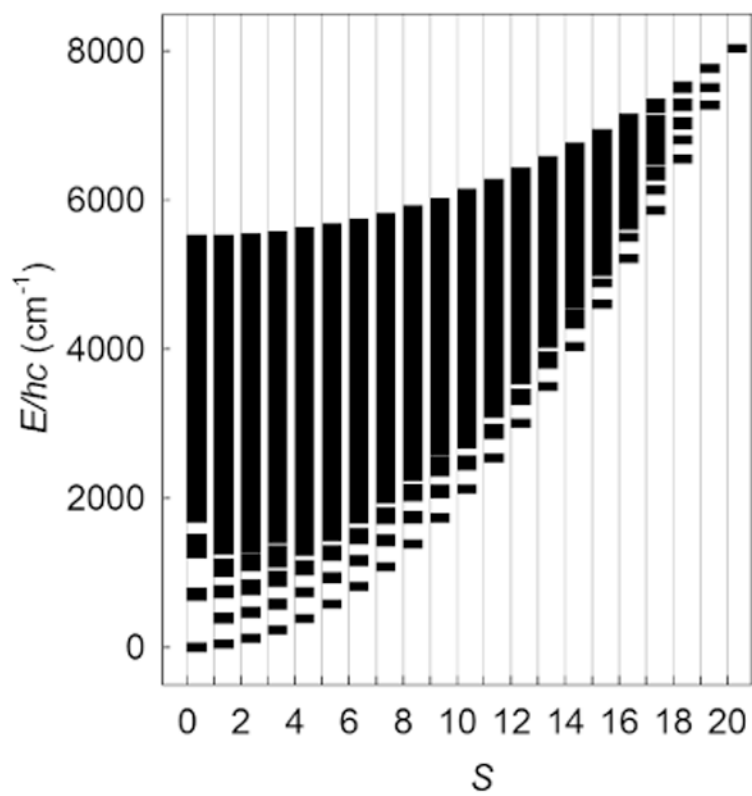
Figure 1.
Ball-and-stick diagrams of **1**, **2**, **3** and **4**.
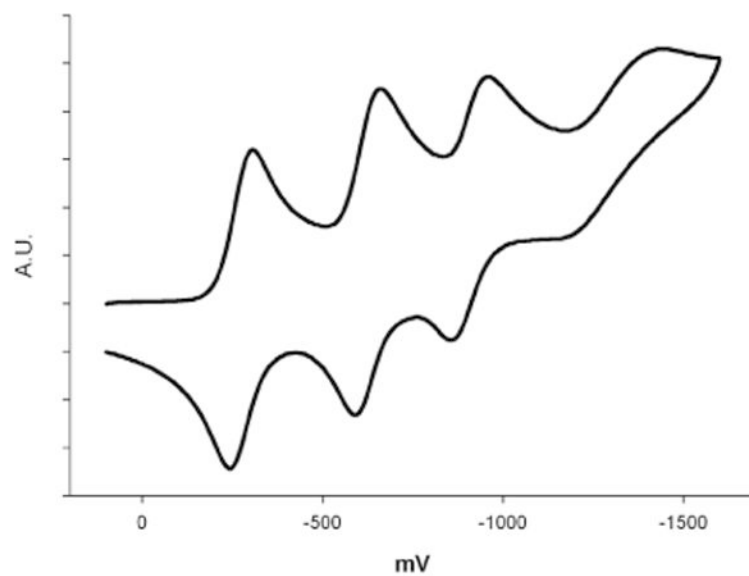
Figure 2.
Cyclic voltamogram of **4** in 0.5 M Bu_4NPF_6/CH_2Cl_2, Pt-disk working electrode, vs Fc/Fc^+.
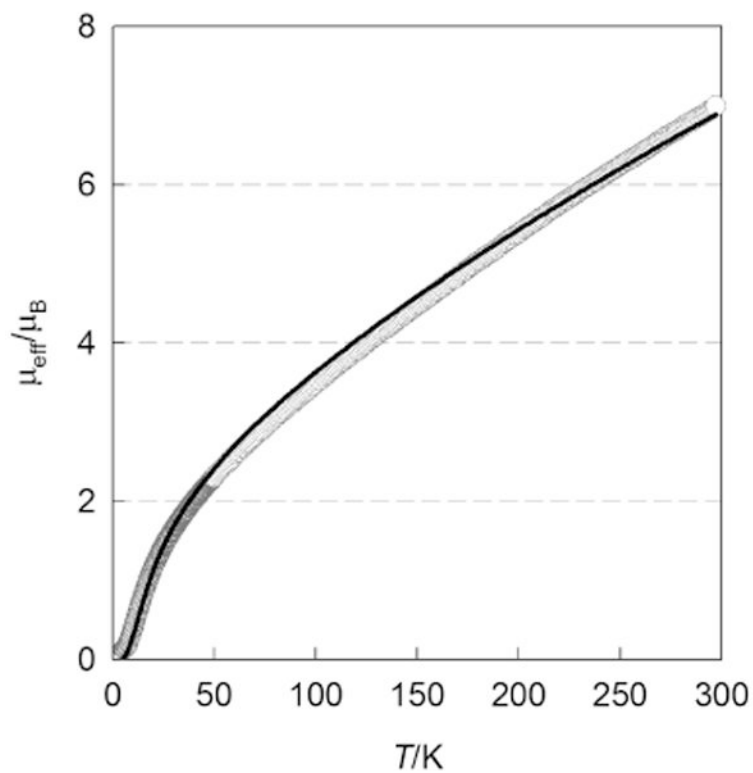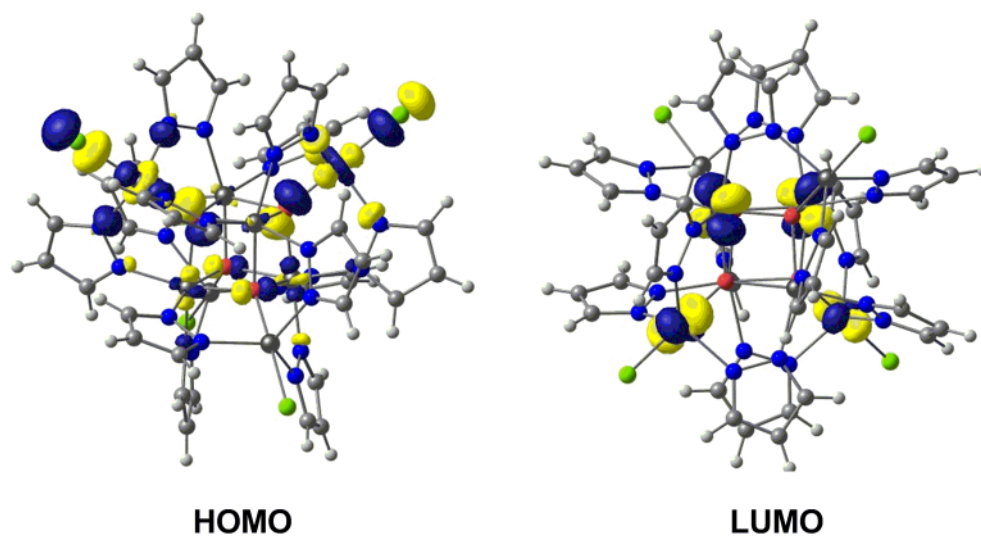
Figure 3.
Temperature dependence of the effective magnetic moment for **1**. Open circles –experimental data, full points – calculated.
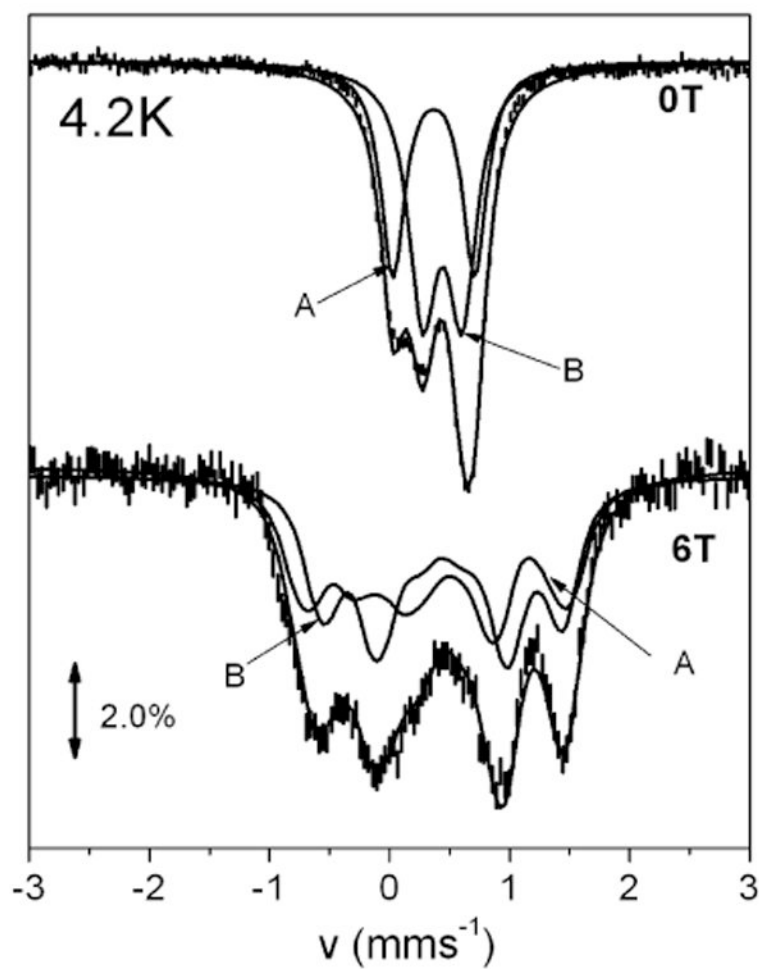
**Figure 4.**
Energy levels versus spin for **1** at B = 0.

Figure 5.
Contour plot of the spin-α HOMO and LUMO for the BS2 state of $Fe_8(\mu_4\text{-O})_4(\mu\text{-pz})_{12}Cl_4$.

Figure 6.
Mössbauer spectra from powdered samples of **1** in the absence or presence of an external magnetic field of 6 T applied perpendicular to the γ-rays. Solid lines are theoretical simulations assuming two species A, B with the parameters quoted in Table 7 (nested model).
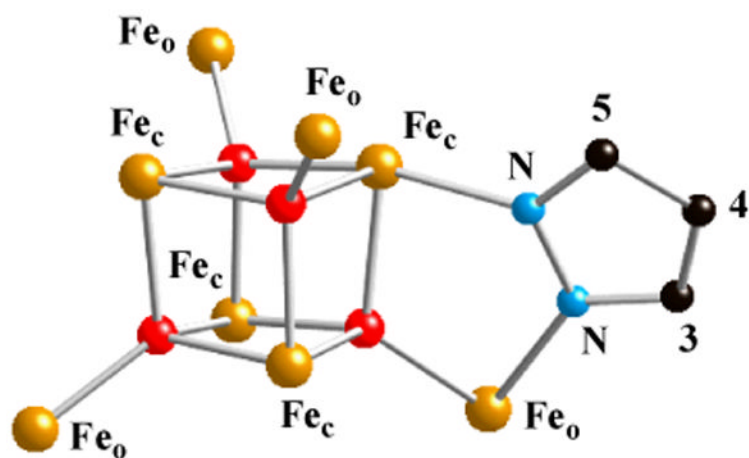
Scheme 1.
The $Fe_8(\mu_4\text{-}O)_4$ motif of complexes **1**-**4,** ferrihydrite, maghemite and ferrihydrite, also indicating the cubane and outer Fe-atoms and numbering scheme for the pyrazolate protons.
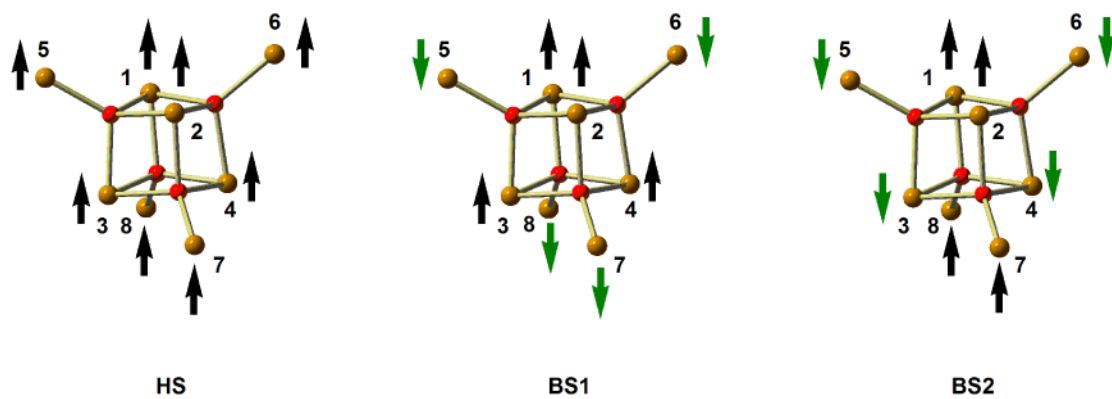
Scheme 2.
Alignment of the spin vectors in **HS**, **BS1** and **BS2** configurations.

Table 1

Crystallographic data for **1**, **2**, **3**, and **4**.

	1	2	3	4
formula	$C_{36}H_{36}Cl_4Fe_8N_{24}O_4$	$C_{36}H_{24}Cl_{16}Fe_8N_{24}O_4$	$C_{48}H_{62}Cl_4Fe_8N_{24}O_5$	$C_{36}H_{36}Br_4Fe_8N_{24}O_4$
crystal size, mm^3	$0.22 \times 0.20 \times 0.08$	$0.29 \times 0.29 \times 0.15$	$0.12 \times 0.08 \times 0.02$	$0.34 \times 0.05 \times 0.04$
fw	1457.49	1870.79	1643.82	1635.33
space group	P2$_1$/n (No.14)	Fd-3 (No. 203)	P-1 (No. 2)	P2$_1$/n (No. 14)
a, Å	12.660(4)	25.934(2)	13.187(2)	12.847(2)
b, Å	21.519(6)	25.934(2)	13.601(2)	21.517(4)
c, Å	20.065(6)	25.934(2)	21.461(3)	20.030(4)
α, °	90	90	87.545(3)	90
β, °	92.976(5)	90	80.550(3)	93.492(3)
γ, °	90	90	71.250(3)	90
V, Å^3	5459(3)	17442(2)	3595.2(10)	5526.5(17)
Z	4	8	2	4
T, K	298(2)	299(2)	302(2)	298(2)
ρ_{calcd}, g cm^{-3}	1.773	1.425	1.518	1.965
reflctns collected/2θ_{max}	23089/46.60	18404/55.96	16013/46.54	27721/50.50
Unique reflctns/$I > 2\sigma(I)$	7838/4631	1058/916	10301/4898	9938/4290
No. of params/restraints	685/0	67/0	833/0	685/0
μ(Mo Kα), mm^{-1}	2.321	1.825	1.772	4.991
F(000)	2912	7360	1668	3200
R1/goodness of fit^{ab}	0.0739/1.080	0.0431/1.292	0.0511/0.864	0.0589/0.933
wR2^c ($I > 2\sigma(I)$)	0.1576	0.1552	0.1036	0.1058

$^a I > 2\sigma(I)$. R1 = $\Sigma||F_O| - |F_C||/\Sigma|F_O|$.

^{b} GooF = $[\Sigma[w(F_O^2 - F_C^2)^2]/(n - p)]^{1/2}$.

^{c} wR2 = $[\Sigma[w(F_O^2 - F_C^2)^2]/\Sigma[w(F_O^2)^2]]^{1/2}$, where $w = 1/\sigma^2(F_O^2) + (aP)^2 + bP$, $P = (F_O^2 + 2F_C^2)/3$.

Table 2

Selected Bond Distances (Å) and Interatomic Angles (°) for **1**, **2**, **3**, and **4**.

	1	2	3	4
$Fe_c - O$	2.032(6)-2.066(7)	2.047(2)	2.028(5)-2.066(5)	2.033(6)-2.060(6)
$Fe_c - N$	2.044(9)-2.086(8)	2.101(3)	2.044(7)-2.080(7)	2.048(9)-2.090(8)
$Fe_c \cdots Fe_c$	3.067(2)-3.091(2)	3.073(2)	3.055(2)-3.112(2)	3.056(2)-3.090(2)
$Fe_c - O - Fe_c$	96.5(3)-98.4(3)	97.3(2)	96.6(2)-99.0(2)	96.5(2)-98.7(3)
$O - Fe_c - O$	81.1(3)-82.7(3)	82.2(2)	80.7(2)-82.7(2)	81.1(2)-82.9(2)
$Fe_o - O$	1.940(7)-1.960(6)	1.930(4)	1.950(5)-1.970(5)	1.943(6)-1.954(6)
$Fe_o - X$	2.271(4)-2.274(4)	2.293(2)	2.284(2)-2.291(2)	2.421(2)-2.425(2)
$Fe_o - N$	2.003(9)-2.038(10)	2.028(3)	2.002(7)-2.034(6)	2.008(9)-2.048(9)
$O - Fe_o - X$	176.9(2)-179.5(2)	180.0(1)	177.7(2)-179.4(2)	176.6(2)-178.9(2)
$N - Fe_o - N$	114.1(4)-124.4(4)	119.6(1)	114.5(3)-123.7(3)	113.5(3)-125.2(3)
$Fe_o \cdots Fe_o$	5.841(3)-5.888(2)	5.843(2)	5.808(2)-5.954(2)	5.835(2)-5.895(2)
$Fe_o \cdots Fe_c{}^a$	3.425(2)-3.481(2)	3.4432(8)	3.437(2)-3.488(2)	3.426(2)-3.487(2)
$Fe_o \cdots Fe_c{}^a$	5.462(2)-5.483(3)	5.460(1)	5.472(2)-5.491(2)	5.457(2)-5.484(2)

[a] There are three short and one long $Fe_O \cdots Fe_C$ distances per Fe-atom, between the verteces of co-centrical tetrahedra formed by the four Fe_C and four Fe_O atoms, respectively.

Table 3

Comparison of structural and Mössbauer isomer shift data.

	1, 2, 3, 4[a]	Maghemite[b]	Ferrihydrite[c]	Magnetite[d]
Fe_c-O	2.028-2.066	2.015-2.104	1.96-2.14	2.140
$Fe_c\cdots Fe_c$	3.055-3.112	2.894-3.012	2.91-3.20	2.968
Fe_c-O-Fe_c	96.5-99.0	87.9-95.2	85.8-102.5	87.78
$O-Fe_c-O$	80.7-82.9	84.7-93.1	73.5-91.0	92.18
δ, mm s^{-1}	0.32(2), 293 K	0.37(5), 293 K	0.35(1), 293 K	$Fe^{2+/3+}$; 0.67, 298 K

[a]This work;

[b]reference 35;

[c]reference 34;

[d]reference 36.

Table 4

[^1]H-nmr data for **1 – 4**.

Compound	[^3]H	[^4]H	[^5]H
1	10.5	42.2	3.5
2	13.7	-	8.6
3	8.6	27.7 (Me[^4])	3.8
4	10.7	42.9	1.0

Table 5

Cyclic Voltemmetric data for complexes **1-4** in dichloromethane at 298 K.

		Potential, V			
		$E_{1/2}(1)$	$E_{1/2}(2)$	$E_{1/2}(3)$	$E_{1/2}(4)$
$Fe_8(\mu_4\text{-}O)_4(\mu\text{-pz})_{12}Cl_4$	**1**	-0.43^a	-0.78^a	-1.07^a	-1.38^a
$Fe_8(\mu_4\text{-}O)_4(\mu\text{-4-Cl-pz})_{12}Cl_4$	**2**	-0.42	-0.67	-0.96	-1.25
$Fe_8(\mu_4\text{-}O)_4(\mu\text{-4-Me-pz})_{12}Cl_4$	**3**	-0.58	-0.91	-1.20	-1.55
$Fe_8(\mu_4\text{-}O)_4(\mu\text{-pz})_{12}Br_4$	**4**	-0.33	-0.62	-0.89	-1.16

[a] Data from reference 20.

Table 6

Computed net spin densities and total energies of Fe_c and Fe_O centers.

	$\rho(Fe_c)$	$\rho(Fe_o)$	$<S^2>$	E / au
BS1(M_S=0)	4.18	-4.03	19.47	-4055.4684
BS2(M_S=0)	±4.20	±4.03	19.54	-4055.4578
HS(M_S=20)	4.18	4.03	420.07	-4055.4323

Table 7

Mössbauer hyperfine parameters of **1** at 4.2 K (293 K) for the two different deconvolution models.

Model	Site	δ (mm s⁻¹)[a]	|ΔE_Q|(mm s⁻¹)[b]	η	Assignment
Nested	A	0.37 (0.25)	0.68 (0.65)	<0.6	Fe_o
	B	0.44 (0.32)	0.33 (0.30)	<0.7	Fe_c
Crossed	A	0.32 (0.19)	0.57 (0.52)	<0.6	Fe_o
	B	0.50 (0.36)	0.43 (0.38)	<0.3	Fe_c

[a] (±0.01 mms⁻¹),

[b] (±0.02 mms⁻¹)